Remote Sensing of Environment 267 (2021) 112725

Contents lists available at ScienceDirect

Remote Sensing of Environment

journal homepage: www.elsevier.com/locate/rse

# Spatiotemporal variability of global river extent and the natural driving factors revealed by decades of Landsat observations, GRACE gravimetry observations, and land surface model simulations

Shang Gao[a], Zhi Li[a,*], Mengye Chen[a], Peirong Lin[b], Zhen Hong[a], Daniel Allen[c], Thomas Neeson[d], Yang Hong[a,*]

[a] School of Civil Engineering and Environmental Science, University of Oklahoma, Norman, OK, USA
[b] School of Earth and Space Sciences, Institute of Remote Sensing and GIS, Peking University, Beijing, China
[c] Department of Biology, University of Oklahoma, Norman, OK, USA
[d] Department of Geography & Environmental Sustainability, University of Oklahoma, Norman, OK, USA

## ARTICLE INFO

Editor: Menghua Wang

*Keywords:*
Landsat
Global river
GRWL
GSW
GRACE
GLDAS
Correlation analysis
Coincidence analysis

## ABSTRACT

Rivers are among the most dynamic components in Earth's terrestrial water cycle and provide critical ecosystem services. Yet, the spatiotemporal variability of river surface extents remains largely unquantified at the global scale. Satellite remote sensing provides a promising alternative to in-situ observations, which can enable a more comprehensive survey and systematic analysis of global rivers at fine spatial resolutions. The study examines the spatiotemporal variability of river surface extent globally and its natural driving factors, by combining the use of Landsat-based Global Surface Water (GSW) and Global River Widths from Landsat (GRWL) databases. In addition to examining the long-term mean river surface extent in various climate zones, we perform statistical analyses to correlate monthly times series of fractional river extent with the terrestrial water storage (TWS) components obtained from the Gravity Recovery and Climate Experiment (GRACE) satellite observation and the Global Land Data Assimilation System (GLDAS) model simulations. Results show that the spatiotemporal variability of water presence in rivers can be explained well via differentiating climate zones. The analysis also shows that 52.7% of the global maximum river extent is covered by water less than half of time. Changes of fractional river extent are found to be highly correlated with groundwater storage in low- and mid-latitudes, whereas snow melting dominates the river dynamics in high latitudes. By examining the extremes of fractional river extent, we found that the abrupt changes of fractional river extent are well linked to precipitation anomalies in the equatorial, arid, and warm temperate areas. This study offers an innovative perspective to study spatiotemporal dynamics of rivers by combining optical remote sensing (Landsat), gravimetry observations (GRACE), and land surface simulations; and it highlights the significant role of low-flow-generating processes (snow melting, infiltration, and recharge-discharge) in controlling river dynamics in certain regions, which warrants future investigation.

## 1. Introduction

Rivers provide critical ecosystem services for human societies (Vörösmarty et al., 2010), including greenhouse gas exchange with the atmosphere, water purification, flood mitigation, and hydropower generation (Bastviken et al., 2011; Raymond et al., 2013; Tang et al., 2009). As one of the most dynamical components in terrestrial water cycle, rivers expand and retract seasonally and at the synoptic scale following storm events (Jensen et al., 2017; Shaw, 2016). The spatiotemporal variabilities of surface water in rivers continuously interact with hydrological, ecological, and geomorphological processes (Gleason and Smith, 2014; Van Dijk et al., 2016; Yamazaki et al., 2012; Yang et al., 2019). Therefore, a thorough understanding of riverine dynamics in responses to environmental factors is vital for ensuring the continued provision of freshwater ecosystem services (Mueller et al., 2016; Sichangi et al., 2016; Tarpanelli et al., 2018), especially under the ongoing changes in the Earth's climate, land use/cover, and human water use (Abbott et al., 2019).

In terms of water quantity, the characterization of river dynamics has traditionally been built upon streamflow observations from in-situ

---

* Corresponding author.
*E-mail address:* yanghong@ou.edu (Y. Hong).

https://doi.org/10.1016/j.rse.2021.112725
Received 6 April 2021; Received in revised form 19 September 2021; Accepted 28 September 2021

gauges (Gudmundsson et al., 2019), but more recently using the emerging remote sensing technologies (Hou et al., 2020). Proxies for discharge include air- and space-borne measurements of surface velocity; radar altimeters to measure surface-water elevations; space-borne measurements of gravity fluctuations to estimate streamflow; and measurements of surface water extent to derive hydrological persistence (Allen and Pavelsky, 2018; Gleason and Smith, 2014; Pavelsky, 2014; Tourian et al., 2017). As one of the most successful missions by the National Aeronautics and Space Administration (NASA), Landsat has been collecting multispectral images of the Earth at a 30-m spatial resolution for the past 37 years since 1984 (Wulder et al., 2016). Based on Landsat archive, researchers have produced several global scale estimates of surface water extents using high performance and cloud-based computing platform such as Google Earth Engine (Gorelick et al., 2017). For instance, Yamazaki et al. (2014) developed the Global Width Database for Large Rivers using Shuttle Radar Topography Mission Water Body Data. A more refined product, Global River Widths from Landsat (GRWL), was produced by Allen and Pavelsky (2018) for rivers wider than 30 m. Yang et al. (2020) produced the Multi-temporal China River Width dataset, the first 30-m multi-temporal river width dataset for China during 1990–2015, which includes estimates under both seasonal fluctuations and dynamic inundation frequencies. Pekel et al. (2016) generated the Global Surface Water (GSW) dataset by using 3 million Landsat scenes, which essentially indicates whether surface water was present at any location of interest from Mar/1984 to Dec/2020 on monthly basis.

For interpretation and attribution of river dynamics, streamflow monitored by gauges has been the primary source because of the long temporal coverage (Fekete et al., 2015). Numerous studies have investigated the trends and climatic variabilities of streamflow at (sub)continental scales (e.g., Hammond et al., 2020; Hodgkins et al., 2017; Tananaev et al., 2016) and the global scale (Gudmundsson et al., 2019) using gauge observations of streamflow. However, the validity of such analyses is compromised by the heterogeneous nature of gauge observations in terms of spatial density, data quality, and record length. For instance, significant imbalance of in-situ streamflow observations exists between developed and developing regions. Moreover, river discharge has rarely been studied in relation with other terrestrial water storage (TWS) components (e.g., Reager et al., 2014; Gao et al., 2021b) whose estimates have become increasingly available via remote sensing (Save et al., 2016), land surface simulation, and data assimilation (Rodell et al., 2004).

With the Landsat datasets, we can now resolve the aforementioned compromise by quantifying river water extent with high spatial resolution, uniform spatiotemporal coverage, and relatively long record. In this study, we focus on the spatiotemporal variabilities of remotely-sensed, global river extent via combined usage of the two Landsat-based datasets, i.e., GSW and GRWL. We also offer an innovative perspective on global river analysis through the relationship of river water with other TWS components, e.g., groundwater, soil water, and snow water equivalent. The estimates of TWS components are based on the Gravity Recovery and Climate Experiment (GRACE) datasets and GRACE-assimilated land surface model simulations. Our goal here is to examine the dynamics of surface water in rivers and to investigate the natural driving factors via 1) examining the long-term average presence of surface water in rivers of various climate zones globally, 2) examining the correlation of monthly fractional river extent (FracSA) with TWS components in world's major river basins, and 3)linking abrupt changes in FracSA with precipitation anomalies (i.e. wet and dry events) using an event coincidence analysis. The paper is organized as follows: Section 2 describes data used in this study and methodology, Section 3 presents the results and discussion, and Section 4 concludes the study and proposes future directions.

## 2. Data and methods

Our methodology starts with defining an examination extent for global rivers, which should ideally encompass the full range of variability due to various factors, e.g., shifts of river channels over time and channel widening/narrowing during floods/droughts. We utilize the monthly history product of Global Surface Water (GSW) dataset (Pekel et al., 2016) which consists of three values, i.e., water, no water, and no observation at 30-m resolution. Within a 30-year period from Jan/1985 to Jan/2015, the union of all 'water' pixels in the GSW monthly history product is taken and referred to as '*max_extent*' hereafter. *Max_extent* essentially masks all the locations ever detected as water over the whole examination period. In concept, *max_extent* is identical to the GSW maximum extent product except for the shorter period (30 years) here in our analysis, compared to the full-range product (37 years) in GSW. We then use the GRWL river centerline to extract river extent from *max_extent* based on connectivity to the river centerline, meaning isolated water bodies not connected to the centerline are excluded. This approach is similar to how rivers are masked in Allen and Pavelsky (2018). We also exclude reaches that cross lakes/reservoirs (with attribute 'lakeFlag' being one) from the GRWL centerlines. A large search distance of 25,000 m is used to examine connectivity to river centerlines, which is to ensure the full widths of large rivers or anabranching/braided rivers are covered. In addition, we address the cases of rivers widening and touching permanent lakes and/or large reservoirs, by unmasking the *max_extent* with the global dataset HydroLAKES (Messager et al., 2016) (https://hydrosheds.org/page/hydrolakes). Fig. 1 illustrates the resulted maximum river extent with an example in Lena River (65°N, 125°E) along with the GSW monthly history product in June of 2005. It can be found that this method can effectively distinguish river extents from non-river water bodies (the numerous isolated pools) and include the anabranching/braided reaches surrounding the islands and bars. Also, the union of 'water' pixels in 360 frames (12 frames/year × 30 years) of GSW monthly history product removes potential 'no observation' artifacts in each frame (Fig. 1B). Therefore, we believe the finalized maximum river extent provides a very reasonable boundary for our further analyses to calculate water presence only related to "rivers".

### 2.1. *Long-term mean surface water presence*

The long-term mean surface water presence (SWP) is also quantified based on the monthly GSW water history dataset. Within the finalized maximum river extent, surface water presence (SWP) is calculated as the fraction of time when surface water is present in the total period. We use two calculation schemes to account for SWP on monthly and yearly bases, respectively. At a given 30-m pixel, the month-based SWP is produced using the equation below:

$$\mathrm{SWP} = \sum \mathrm{WD} \Big/ \sum \mathrm{VO} \tag{1}$$

where WD is water detection; and VO is valid observation which includes WD and no-water detection. Calculation based on Eq. (1) is performed for each of the 12 months over the 30-year period and the arithmetic mean of the twelve values is then taken as the long-term mean SWP. Instead of the ratio between the total WD and VO over the 30 years, the arithmetic mean of the monthly SWP reduces the effect from the uneven observations among different months. Such calculation of month-based SWP is identical to that of water occurrence in GSW (Pekel et al., 2016), but applied to a shorter period (30 years) than the full 37 years in GSW.

Alternatively, a year-based SWP is calculated by dividing the number of years with at least one WD by the number of years with at least one VO. Month-based and year-based SWP are first calculated at each pixel and then areal-averaged to represent each river reach. HydroBASINS level 7 reaches/catchments (Lehner and Grill, 2013) (https://hydrosheds.org/page/hydrobasins) are used for the areal-averaging because

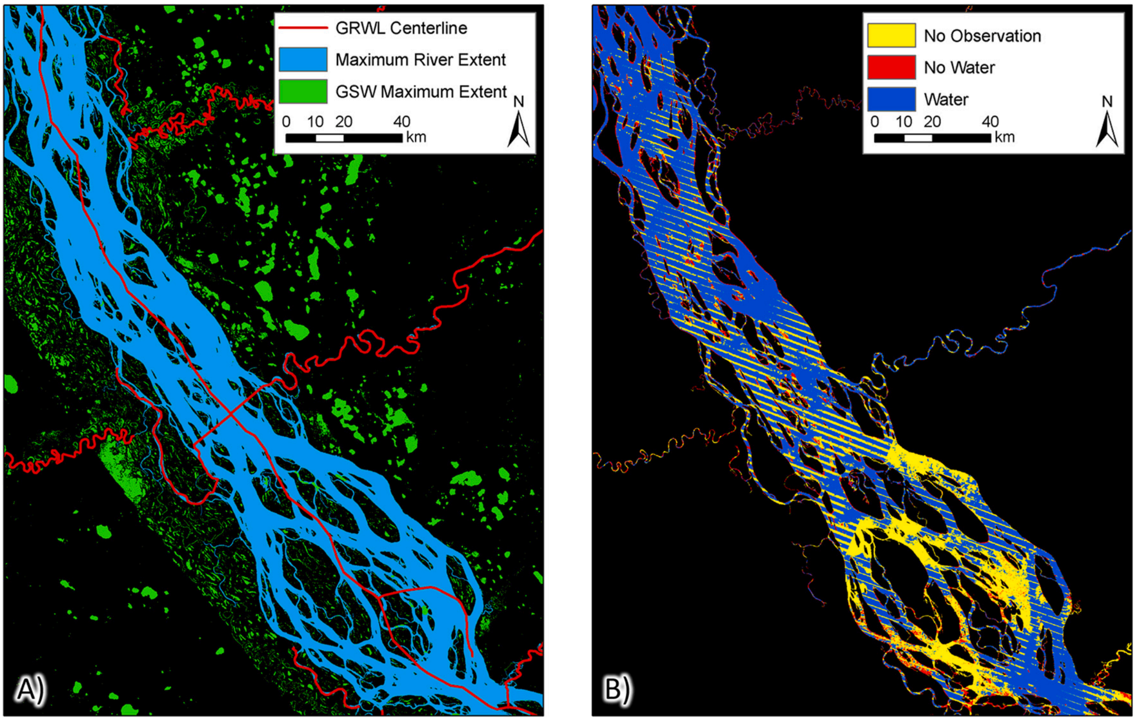

**Fig. 1.** Example of A) the maximum river extent (blue) extracted maximum surface water extent (green) using the GRWL centerline (red) with a search distance of 25,000 m, and B) the GSW monthly history product masked by the maximum river extent in June of 2005. (For interpretation of the references to colour in this figure legend, the reader is referred to the web version of this article.)

the DEM-based catchments can naturally divide river extent at confluences. The Google Earth Engine's parallel processing libraries enable the pixel-wise calculation of long-term mean surface water presence (Azzari and Lobell, 2017; Donchyts et al., 2016).

In this study, we separately examine the long-term SWP in different climate types. In doing so, we use Köppen-Geiger climate classifications (http://koeppen-geiger.vu-wien.ac.at/) (Kottek et al., 2006) based on five main climates: equatorial, arid, warm temperate, snow, and polar. The sub-categories enable a more refined view according to the precipitation and temperature of that region. Fig. 2A to 2C show maps of climate zones defined by the three categories: main, precipitation, and temperature climates, respectively.

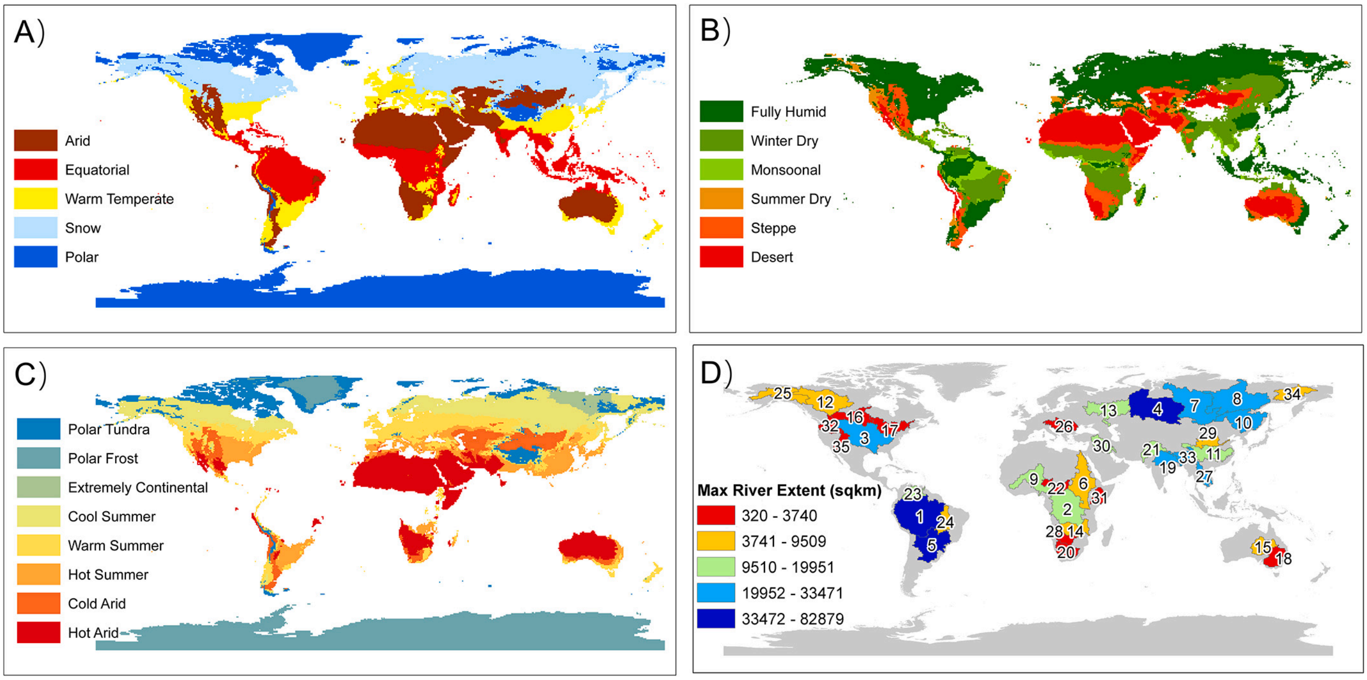

**Fig. 2.** Global view of A) main climate zones, B) precipitation climate zones, C) temperature climate zones and D) area of maximum river extent in 35 large river basins. Labels in D) signify basin ID. Note in C) temperature classification is not applied to the equatorial climates.

### 2.2. *Correlation analysis with terrestrial water storage components*

As a dynamic component in TWS, river water should covary with other TWS components by some lags at various spatial and temporal scales. Here, we define the fractional river extent (FracSA) as the ratio of 'water' pixels over valid observations (sum of 'water' and 'no-water' pixels) within the maximum river extent mask, as showcased in Fig. 1B. FracSA is used instead of the actual water-covered area because the Landsat observations are spatially discontinuous including 'no observation' pixels (Fig. 1B). The monthly FracSA is produced using the GSW monthly water history product for the world's largest 35 river basins (Fig. 2D), whose boundaries are obtained from the total runoff integrating pathway (TRIP) database (Oki and Sud, 1998). The lead/lag correlation analysis is then conducted between the monthly FracSA and the TWS along with its components, including plant canopy surface water (CanopInt), root zone soil water (SoilMoist_RZ), snow water equivalent (SWE), and groundwater storage (GWS). Basic information of the 35 river basins is summarized in Table 1.

The TWS anomaly is based on the 5th generation (RL05) Mascons product provided by the Center for Space Research (Save et al., 2016). This GRACE product is a recently-released local solution developed to minimize the common north-south striping error and spherical harmonic noise. These datasets are provided at monthly intervals and at $0.5^\circ \times 0.5^\circ$ resolution from April 2002 to December 2016 and can be used without post-processing (http://www2.csr.utexas.edu/grace) (Save et al., 2016).

GLDAS is a suit of land surface models that output land surface states and fluxes using parameters obtained/derived from satellite observations, ground observations, and (re)analyses (Rodell et al., 2004). The recently released version 2.2 of GLDAS is well-suited to be utilized along with the GRACE dataset, because GLDAS 2.2 products currently include data assimilation from the GRACE from 2003 to present. Based on mass balance in GLDAS-v2.2, TWS is the sum of GWS, SoilMoist_RZ, SWE, and CanopInt. The daily GLDAS products are acquired from https://hydro1.gesdisc.eosdis.nasa.gov/data/GLDAS/GLDAS_CLSM025_DA1_D.2.2/. The raw data are then spatially averaged over the TRIP basins, temporally averaged, and converted to the monthly anomalies. The analysis is conducted over the period from February 2003 to January 2015. Lagged correlation is calculated between the anomaly times series of TWS storages and FracSA with the former preceding the latter by 0 to 6 months.

### 2.3. *Linking FracSA with hydrologic extremes*

Previous studies have demonstrated strong links between hydrologic inputs and TWS using correlation analysis (Crowley et al., 2006; Frappart et al., 2013) and also with respect to hydrologic extremes like floods and droughts (Sun et al., 2017). The statistical evidence reported in these studies are essentially driven by the mass balance relationship where change in TWS equals to precipitation minus evapotranspiration minus surface runoff. In this study, we also explore the relationship between abrupt changes of FracSA and precipitation anomalies.

One major challenge in Landsat datasets is that they are less representative of the extreme streamflow than the average values due to the spatiotemporal discontinuity (Allen et al., 2020). As a work-around, we conduct an event coincidence analysis (Sun et al., 2017) to link the timings of abrupt changes in FracSA, represented by break points in FracSA time series, and precipitation anomalies based on standard precipitation index (SPI). By doing so, we equate the timings of wet/dry FracSA events with FracSA break points (BPs), i.e., the time when an interruption or abrupt change is made. This approach was originally applied on TWS anomaly times series (Sun et al., 2017), including an empirical mode decomposition (EMD), a break point detection, and finally an event coincidence analysis. The three steps are briefly

**Table 1**

Summary of basic information for the 35 major global river basins.

| ID | Name | Drainage Area (km$^2$) | Maximum River Area (km$^2$) | Major Climate Type | Tailored Period | Mean Observation Rate |
|---|---|---|---|---|---|---|
| 1 | AMAZON | 6,108,480 | 82,879 | Equatorial | 1985–2015 | 54% |
| 2 | CONGO | 3,710,250 | 18,103 | Equatorial | 2000–2015 | 47% |
| 3 | MISSISSIPPI | 3,244,560 | 23,740 | Warm Temperate | 1985–2015 | 69% |
| 4 | OB | 2,965,730 | 59,320 | Snow | 2000–2015 | 33% |
| 5 | PARANA | 2,998,410 | 50,579 | Warm Temperate | 1985–2015 | 77% |
| 6 | NILE | 2,888,270 | 5633 | Arid | 2000–2015 | 74% |
| 7 | YENISEY | 2,588,220 | 24,535 | Snow | 2000–2015 | 28% |
| 8 | LENA | 2,342,790 | 29,213 | Snow | 2000–2015 | 29% |
| 9 | NIGER | 2,110,740 | 12,056 | Arid | 2000–2015 | 64% |
| 10 | AMUR | 1,867,270 | 29,536 | Snow | 2000–2015 | 51% |
| 11 | CHANGJIANG | 1,823,410 | 19,951 | Warm Temperate | 2000–2015 | 66% |
| 12 | MACKENZIE | 1,679,780 | 9509 | Snow | 1985–2015 | 33% |
| 13 | VOLGA | 1,383,890 | 14,449 | Snow | 2000–2015 | 46% |
| 14 | ZAMBEZE | 1,296,430 | 9007 | Warm Temperate | 1990–2015 | 64% |
| 15 | LAKEEYRE | 1,241,960 | 6582 | Arid | 1990–2015 | 94% |
| 16 | NELSON | 1,049,830 | 2954 | Snow | 1985–2015 | 49% |
| 17 | ST-LAWRENCE | 873,250 | 3401 | Snow | 1985–2015 | 57% |
| 18 | MURRAY | 1,065,410 | 1424 | Arid | 1990–2015 | 85% |
| 19 | GANGES | 1,026,950 | 24,229 | Warm Temperate | 1990–2015 | 60% |
| 20 | ORANGE | 994,350 | 725 | Arid | 1990–2015 | 70% |
| 21 | INDUS | 966,691 | 15,424 | Arid | 2000–2015 | 80% |
| 22 | CHARI | 895,085 | 1818 | Equatorial | 2000–2015 | 62% |
| 23 | ORINOCO | 954,701 | 14,595 | Equatorial | 2000–2015 | 63% |
| 24 | TOCANTINS | 858,704 | 9298 | Equatorial | 1985–2015 | 67% |
| 25 | YUKON | 847,109 | 8655 | Snow | 2000–2015 | 31% |
| 26 | DANUBE | 804,912 | 3740 | Warm Temperate | 2000–2015 | 57% |
| 27 | MEKONG | 798,977 | 28,280 | Equatorial | 2000–2015 | 71% |
| 28 | CUBANGO | 789,009 | 384 | Arid | 1990–2015 | 67% |
| 29 | HUANGHE | 783,467 | 5648 | Arid | 2000–2015 | 67% |
| 30 | EUPHRATES | 759,092 | 11,848 | Arid | 2000–2015 | 71% |
| 31 | JUBBA | 735,993 | 320 | Arid | 2000–2015 | 64% |
| 32 | COLUMBIA | 720,785 | 2272 | Warm Temperate | 1985–2015 | 57% |
| 33 | BRAHMAPUTRA | 654,169 | 33,471 | Polar | 2000–2015 | 71% |
| 34 | KOLYMA | 636,512 | 8889 | Snow | 2000–2015 | 26% |
| 35 | COLORADO | 623,896 | 1622 | Arid | 1985–2015 | 78% |

introduced as follows.

#### 2.3.1. Empirical mode decomposition (EMD)

EMD is a sifting process that retrieves zero-mean, oscillatory modes called intrinsic mode functions (IMFs) from a time series. The EMD is necessary for aiding the subsequent BP analysis due to the following challenges. First, FracSA extremes might occur irregularly, meaning the wet events show high intensity and short duration whereas dry events feature slow onset and longer duration. Second, the FracSA extremes can mix with seasonal and/or long-term trends. The traditional BP detection relies on an assumed existence of an underlying seasonal cycles, which is not always true; and the removed seasonal cycles might consequently amplify or weaken the extremes.

Compared to the more commonly used wavelet analyses, EMD is entirely data-driven and decomposes a time series without prior knowledge about the time series (Wu and Huang, 2004). EMD algorithms are described in greater detail in (Huang et al., 1998). The outputs of EMD are several IMFs and a residual term, which sum to exactly the original time series. This study adopts EMD similarly to Sun et al. (2017), where the ensemble EMD by (Wu and Huang, 2004) is used to avoid mode mixing and then the critical frequency associated with known floods and droughts is used to facilitate the break point detection.

#### 2.3.2. Break point (BP) detection

Following the EMD, an BP detection algorithm, breaks for additive season and tend (BFAST), is used (Verbesselt et al., 2010). One important input of BFAST is the minimum interval between two adjacent BPs, which is determined based on the critical frequency detected in the EMD analysis. The R package, BFAST, is used (Verbesselt et al., 2010).

#### 2.3.3. Event coincidence analysis

We then use event coincidence analysis (ECA) to quantify the match of timings between precipitation anomalies and abrupt FracSA changes. For precipitation anomalies, standard precipitation index (SPI) is calculated based on the precipitation forcing fields in GLDAS v2.1 (meteorological fields are not currently included in GLDAS v2.2) available from January 2000 to present, which are from the disaggregated Global Precipitation Climatology Project (GPCP) V1.3 Daily Analysis. Monthly SPI time series is calculated from basin-averaged rainfall cumulated over 3 months (i.e. SPI3) using the R package SPEI (Vicente-Serrano et al., 2010). We use a threshold of $1(-1)$ to represent floods (droughts) of moderate severity.

ECA is nonparametric and only requires knowledge of the timing of events. Given two binary event time series, $ES_A$ and $ES_B$, ECA counts how often events in those two series co-occur, within a user-defined sliding window $\Delta T$. The sliding window $\Delta T$ is used to accommodate irregularity in event concurrence times. For the purpose of this study, we use a so-called precursor coincidence rate, as defined below

$$r_p = \frac{1}{N_A}\sum_{i=1}^{N_A} H\left(\sum_{j=1}^{N_B} I_{[0,\Delta T]}\left(t_i^A - t_j^B\right)\right) \tag{2}$$

where $N_A(N_B)$ is the number of events; $t^A$ ($t^B$) is event occurrence time; $H$ is the Heaviside step function; and $I_{[0,\Delta T]}$ is an indicator function that equals to 1 when the argument falls within the interval $[0, \Delta T]$ and 0 otherwise. If $ES_A$ represents FracSA event series and $ES_B$ represents SPI anomaly series, then $r_p$ measures the fraction of FracSA events that are preceded by at least one SPI anomaly. For the FracSA, times of abrupt changes (BPs) are used to form event series. Sliding windows of six months are attempted (Eq. 2) in ECA calculations between FracSA and SPI. We use the R package CoinCalc for ECA analysis (Siegmund et al., 2017).

## 3. Results and discussion

### 3.1. River SWP results

We find that 52.7% (22.2%) of global river extent has areal-averaged month-based (year-based) SWP values less than 50% (Fig. 3). Across the latitudes, river area is spatially concentrated between 30 N and 60 N. The longitudinal distribution of river area generally reflects the distribution of land. As expected, year-based SWP is greater than month-based SWP, as a year is counted as having water if at least one month having water present. The latitudinal profiles of both SWP estimates show that the river water is most frequently present at higher latitudes of north hemisphere and near the equator. The high SWP of rivers near 60S is not as significant due to their small spatial extent.

Furthermore, SWP and maximum river area vary in different climate zones categorized based on 1) main climate types, 2) precipitation, and 3) temperature (Fig. 4). The SWP metrices indicate the average temporal behavior of rivers while the maximum river area represents the spatial distribution of rivers under different climates. Across the three types of climate zone classifications, the month-based and year-based SWP share similar spatial patterns indicating the robustness of both metrices. This also implies the inter-annual variabilities are probably more dominant than intra-annual variabilities in most rivers globally. For the main climate zones, the snow and polar areas feature the highest SWP with the other climate zones showing equally lower SWP. As opposed to rain storms, snow-melting generates low, gradually-varied streamflow that sustains over a long period of time. For precipitation climate zones, river area shows larger range of variabilities than SWP. Fully humid areas have the largest river area globally followed by winter dry, monsoonal, steppe, desert and summer dry areas. In contrast, the rivers in desert climates have limited river area and the rarest presence. For temperature climate zones, hot areas in general show lower SWP (Fig. 4E) and smaller river area (Fig. 4F) than cold area, according to the description of temperature climate zones in (Kottek et al., 2006). The polar areas see high SWP but minimal river extents, as most surface water is frozen all year long. Note that temperature classification is not applied to the equatorial climate (Kottek et al., 2006), as shown in Fig. 2C. In summary, the distribution of long-term mean SWP and river area across climate zones reflect the effects of various hydro-meteorologic processes like snow melting, precipitation, and evapotranspiration.

### 3.2. Correlation analysis results

Prior to the correlation and event coincidence analysis, we first examine the quality of Landsat observations in TRIP basins. Fig. 5 shows that the coverage of Landsat observations improved and became steady at different points in time for different basins, i.e., 1985 for Amazon, around 2000 for Nile and 1990 for Zambeze. Therefore, we accordingly tailored the examination period for each basin in the correlation and event coincidence analyses (Table 1), so that most basins except for those in the cold areas (due to polar nights) end up with fair ($>$ 50%) mean observation rate (percentage of observed out of the total number of pixels).

Fig. 6A to 6D show the optimal correlations along with the corresponding lags between FracSA and TWS, GWS, SoilMoist_RZ, and CanopInt, respectively. Note that only the results with statistical significance are shown ($p$ value $<0.05$). Overall, correlations of FracSA with TWS and the three components share similar spatial pattern where the value is relatively low at high latitudes (>60 N) but high in low- and mid-latitudes (60S to 60 N) with small lags. The correlation of FracSA with TWS is fair, with 17 basins reaching above 0.5 and 7 basins above 0.7; and 13 (5) out of the 17 (7) basins are in low- and mid-latitudes. The results for GWS and SoilMoist_RZ are similar with 17 and 20 basins showing correlation above 0.5 with FracSA, respectively. Typical examples are the Ganges (#13) and Brahmaputra (#33) where correlations of FracSA vs GWS, SoilMoist_RZ, and CanopInt are equally high ($\geq$

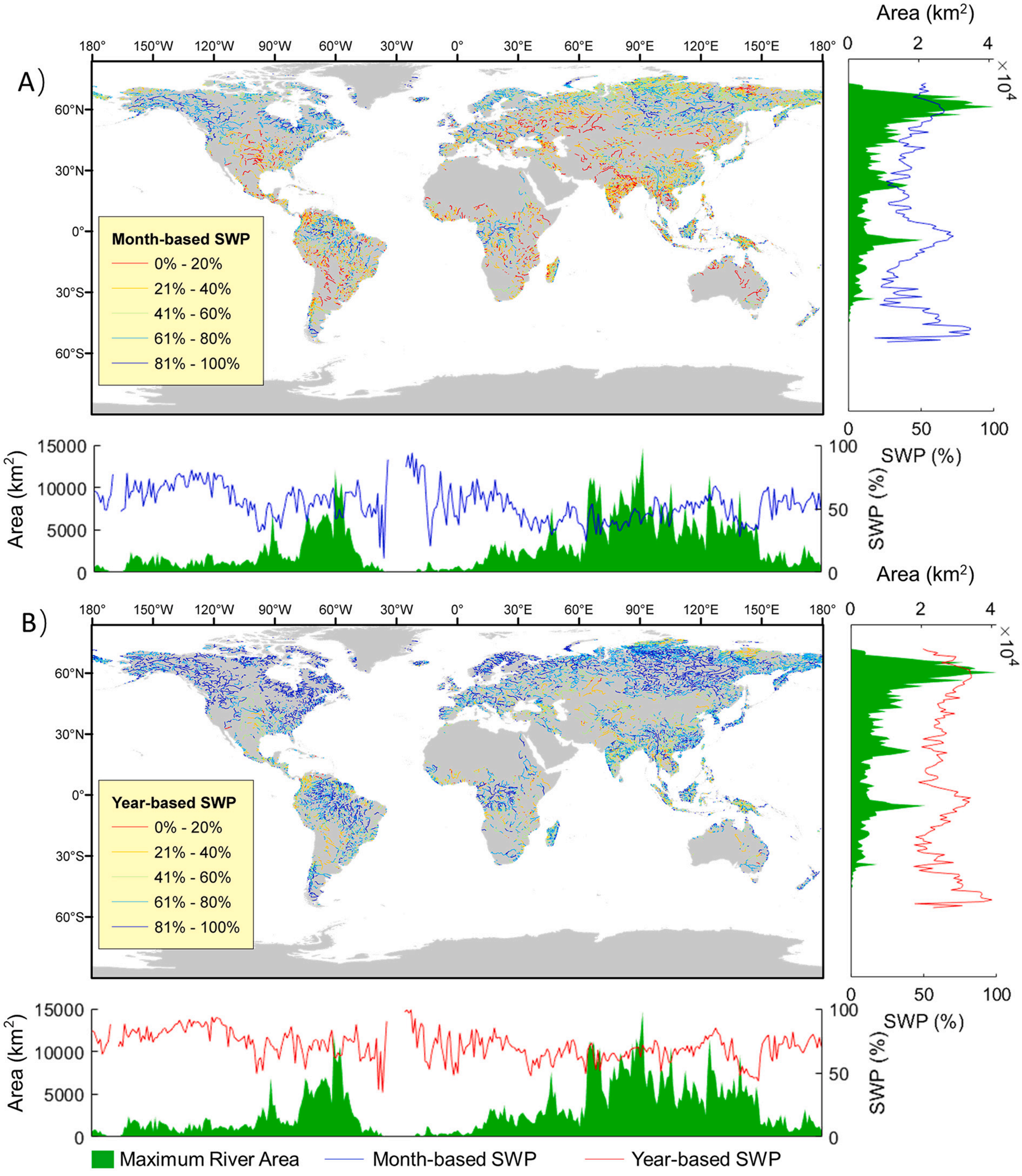

**Fig. 3.** Month-based (A) and year-based (B) long-term surface water presence of global river reaches (HydroBASINS level 7 reaches) from 1985 to 2015. In the maps, pixel values encompassed by maximum river extent are averaged over HydroBASINS level 7 catchments to represent SWP of the corresponding reaches. Only reaches with positive maximum river extent are shown. Plots show the latitudinal and longitudinal profiles of SWP and maximum river extent using bin width of 1°.

0.8) at small lags (≤2 months). The hydrologic regime in this region is dominated by the Indian monsoon, which is concentrated in the summer months and amounts to 60–90% of the annual precipitation (Forootan et al., 2016). This highly seasonal, intense hydrologic inputs might be the cause for the three storages to highly co-vary. In majority of the basins (25 out of 35), the optimized lags of FracSA behind GWS are the smallest followed by SoilMoist_RZ and then CanopInt, with most exceptions having statistically insignificant CanopInt results, including OB (# 4), Yenisey (#7), Lena (#8), Changjiang (#12), 25 Yukon (#25), and Colorado (#35). Such patterns indicate how recharge-discharge process affects river dynamics — throughfall infiltrates into soils, then percolates into aquifers and finally discharges at rivers. However, in these 25 basins, the lags of FracSA behind CanopInt are not always the largest (as they should be in the recharge-discharge process) but sometimes equal to lags of FracSA behind SoilMoist_RZ, e.g., Orange (#20), Tocantins (#24), and Cubano (#28). One potential cause is that only part of CanopInt is involved in the recharge-discharge process with the remaining portion contributing to rivers as surface runoff. Also, the monthly timestep may be too coarse to differentiate variabilities in SoilMoist_RZ and CanopInt especially when the infiltration processes occur at a higher rate. The correlation results for SWE are not shown due to lack of Landsat observations in winter months when most of SWE

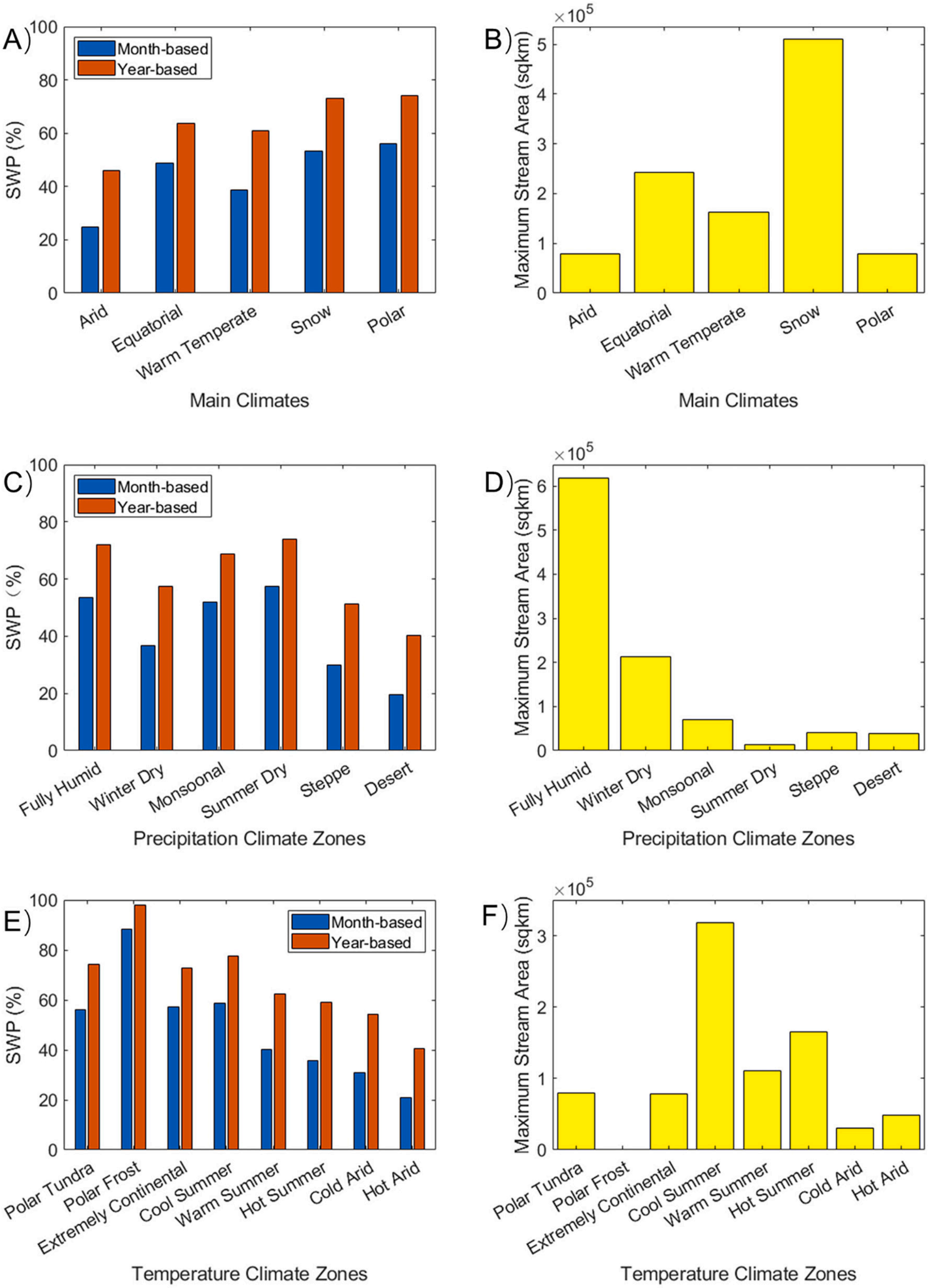

**Fig. 4.** Surface water presence and area of maximum river extent in main climate zones (A, B), precipitation climate zones (C, D) and temperature climate zones (E, F).

change (increase) occurs.

To further corroborate the correlation analysis, we investigate the differential time series of TWS storages and FracSA, which is the current month value minus the previous month value. Latitudinal profiles of zonally averaged differential TWS storages and differential FracSA are examined for the four seasons (Fig. 7). The latitudinal profile of differential TWS closely follows that of differential GWS except for high latitudes where SWE is critical. The highest and the lowest values of differential TWS and GWS are mainly centered on 15 N and 15S. Latitudinal profiles of differential TWS and GWS also largely agree with

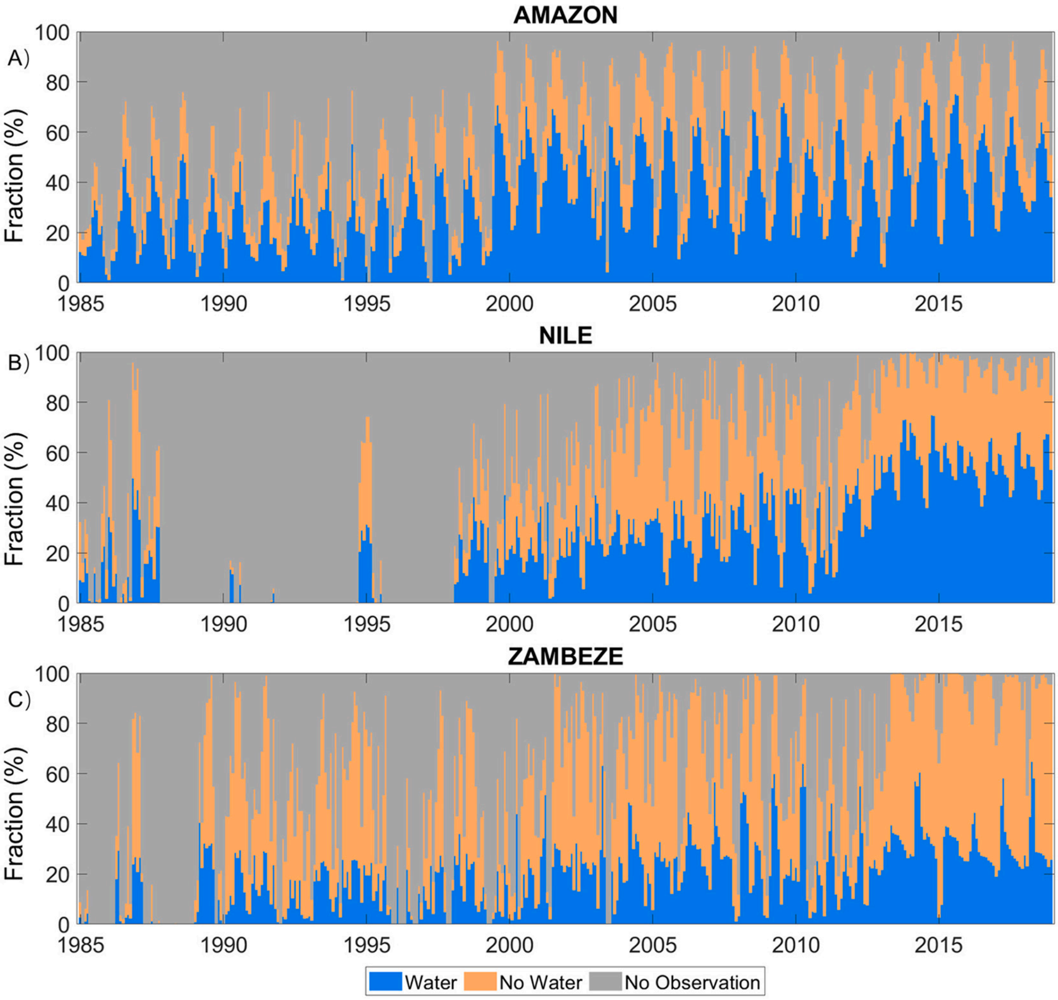

**Fig. 5.** Time series of data composition of Global Surface Water monthly history product (water, no water, and no observation) in the maximum river extent for three example basins, A) Amazon, B) Nile, and C) Zambeze.

differential FracSA expect for in the high latitudes. This analysis allows us to partly see the effect of SWE on FracSA: SWE begins contributing to TWS near 40 N during December–January-February; followed by a subsequent drop in SWE/TWS values during spring (MAM) as snowpack melts, infiltrates into the soils, recharges the groundwater, and increases the FracSA (north of 45 N).

### *3.3. Event coincidence analysis (ECA) results*

The aim of EMD is to facilitate BP detection by identifying the critical frequency associated with floods/droughts. This frequency then determines the minimal interval as an important input for subsequent BP detection. Across all 35 basins, IMF2 resembles an annual cycle with an averaged mean period (separation between any two highs or lows) of 9.7 months. IMF3 is at a biennial scale (averaged mean period = 23 months). Fig. 8 shows FracSA anomaly time series along with their IMF3 in four example basins. In Amazon, IMF3 shows cyclic patterns and correspond with droughts in 2005 (Chen et al., 2009) and 2010 (Frappart et al., 2013), dry year 2007 (Frappart et al., 2013), extreme flood in 2009 (Chen et al., 2010), and austral summer in 2011 (Espinoza et al., 2013) and 2013 (CRED, 2017) (https://public.emdat.be/). Unlike Amazon, the Mississippi basin shows signs of non-stationarity in the FracSA anomaly series, with a consistently dry period before year 2008 and a wet period from 2008 to 2011. The extreme flood in 2011 (Reager et al., 2014) and extreme drought in 2012 (Hoerling et al., 2014) are clearly identifiable from IMF3. The drought-ending wet event in 2008 and wet year 2013 can also be found (CRED, 2017). The Zambeze basin is known for the strong annual cyclic pattern in its TWS (Ahmed et al., 2014), which can be discerned from the shape of IMF3. We can clearly identify a wet event in 2003 that separates the prolong drought from 2002 to 2005 (Winsemius et al., 2006), followed by a wet event in 2006; afterwards the basin enters a period when wet and dry events occurred alternately on an annual basis. In the Murray Darling basin, the ending of the prolonged drought in 2010 can be seen (Leblanc et al., 2012); the wet events in 2012 and 2014–2015, and dry year 2011 can also be identified (CRED, 2017). Overall, EMD can accommodate irregularity of FracSA extremes and the resulted IMF3 align well with known floods/droughts.

As a result of the BP detection, the short-term trends comprise of periods separated by abrupt changes (BPs), as shown in Fig. 9. In Amazon, the severe droughts in 2005 and 2010 are noticeable from the very low SPI values, which also correspond to two downward trends of FracSA (Fig. 9A). One can also tell the 2006 wet year, as indicated by the high SPI, interrupted the downward trend started by the 2005 drought, which was however immediately followed by another dry year 2007 (Frappart et al., 2013). These event series create a sequence of sharp rising and declining trends. Another example can be found for the extreme flood in 2009 (Chen et al., 2010) followed by the extreme drought in 2010 (Maeda et al., 2015), creating a steep downward trend. Short-term trends often start and/or end with sudden jumps, for instance, the positive jumps related to 2009 and 2011.

For the Mississippi River basin, the most discernable event is the

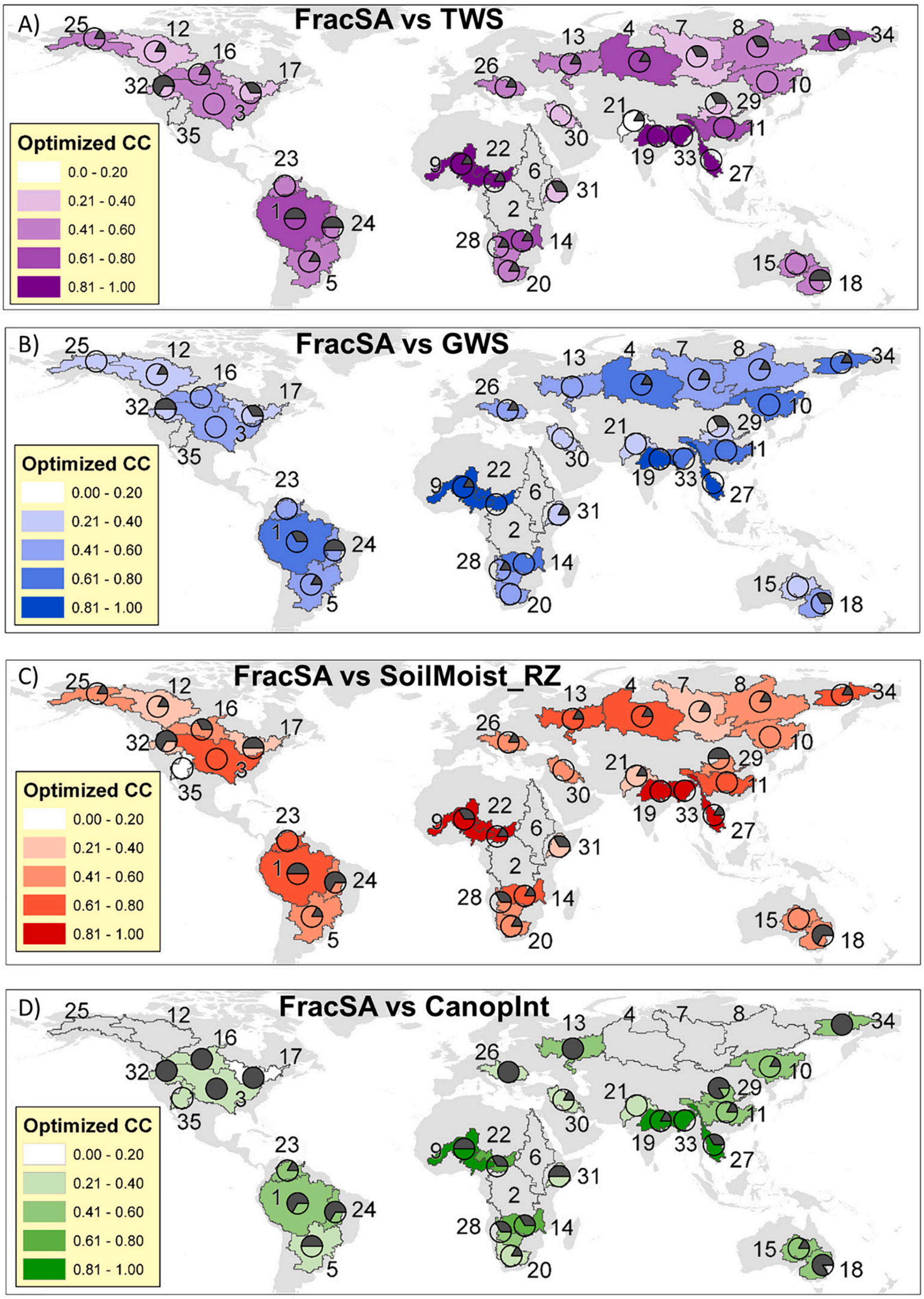

**Fig. 6.** Maps of the 35 river basins colored by optimal lagged correlation of basin-averaged (A) terrestrial water storage (TWS), (B) groundwater storage (GWS), (C) root-zone soil water (SoilMoist_RZ), and (D) plant canopy surface water (CanopInt) vs fractional river extent (FracSA). Only correlation results with $p$ values $<0.05$ are displayed. Pie charts indicate lags (clockwise) between the TWS (components) and FracSA, which are normalized by 6 months. Zero-lags are shown as clear circles.

severe Central U.S. flash drought in 2012 (Hoerling et al., 2014) as indicated by both the low SPI and the sharp declining trend of FracSA (Fig. 9B). BPs and SPI anomalies can also be associated with the extreme Midwest flood in 2011 (Reager et al., 2014) and the flood at the beginning of 2008. It should be noted that hurricane-related wet year 2005 is only detected by SPI but not by FracSA BPs. A possible reason can be that the BP detection fails to differentiate mixed signals from BPs and persistent, seasonal components which are in this case the regular annual cycles from 2000 to 2008.

The Zambeze River basin is characterized by the frequent precipitation variation as indicated by the 18 SPI anomalies (Fig. 9C). A drought started in 2002, intercepted by a wet event in 2003, and continued till 2005, followed by a 3-year wet period till 2008; afterwards, the basin enters a relatively stationary state with wet and dry events occurring almost biannually. In the Murray Darling basin, Australia's millennium drought from 2001 to 2008 can be clearly identified by the long downward trend of FracSA (Fig. 9D). We can also tell the ending of this prolong drought from the sudden jump of FracSA caused by a significant wet event in 2010 (Leblanc et al., 2012). After 2011, the region encountered a sequence of alternating wet and dry events indicated by the SPI anomalies. In summary, the FracSA BPs and the SPI anomalies can be explained by the reginal hydrometeorology and associated with known wet/dry events.

With BPs of FracSA detected, the coincidences between FracSA and SPI anomalies are quantified for each of the 35 river basins via ECA (Fig. 10). The precursor coincidence rates ($r_p$ in Eq. 2) measure the proximity in timings between the preceding (as much as six months) SPI anomalies and the FracSA BPs. The ECA results should be interpreted in

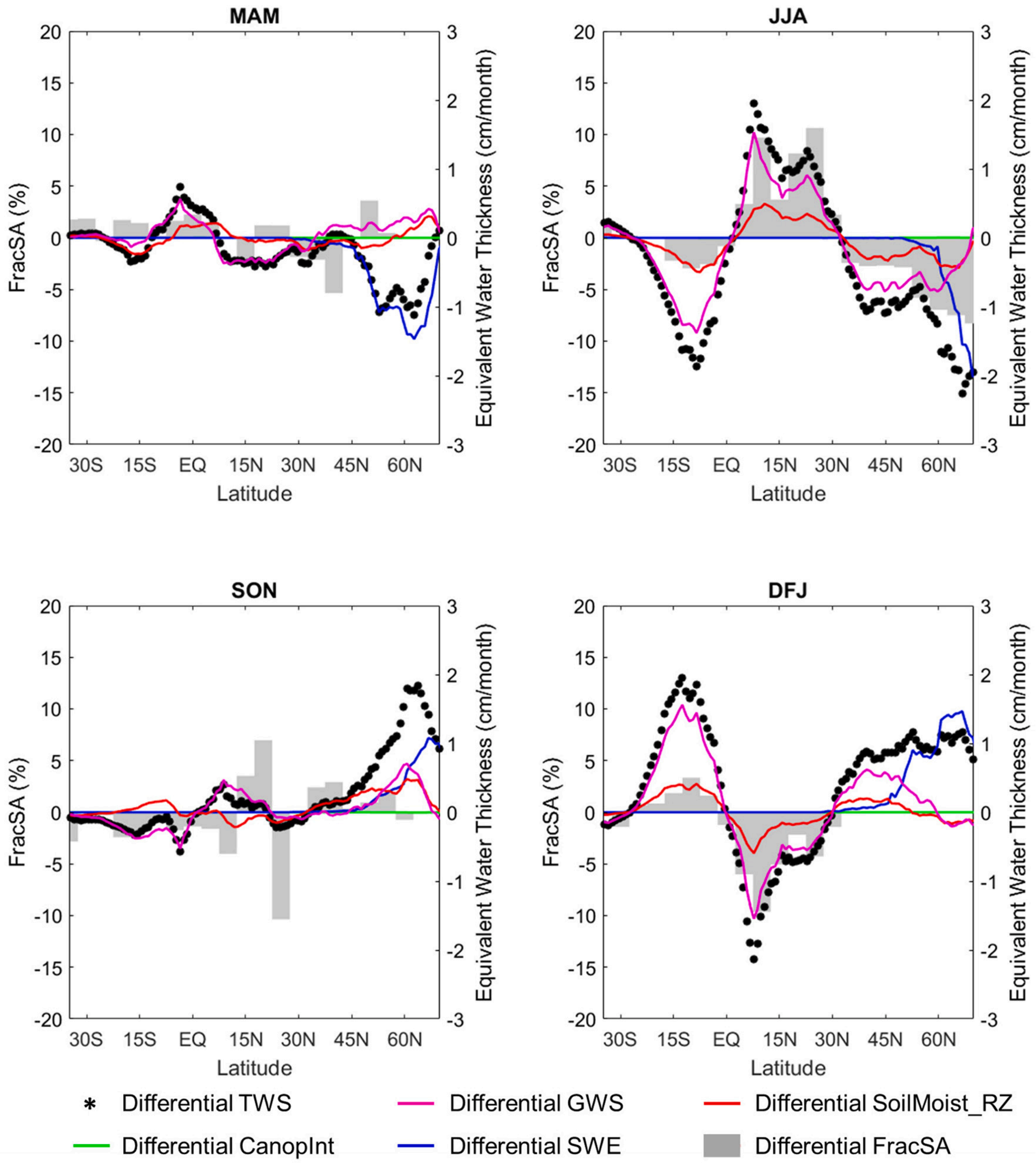

**Fig. 7.** Latitudinal profiles of zonally averaged differential TWS and its storage components (GWS, SoilMoist_RZ, CanopInt, and SWE) along with differential fractional river extent for the four seasons, March–April-May (MAM), June–July-August (JJA), September–October-November (SON), and December–January-February (DJF).

conjunction with the number of BPs, as more BPs imply higher statistical significance of ECA results. There are 23 basins with more than 6 BPs (0.4 BP/year), among which 17 basins show high ($\geq 0.8$) $r_p$. Three basins show null coincidence values either due to statistical insignificance (Brahmaputra basin) or unavailable precipitation data (St-Lawrence and Jubba basins). Fifteen basins show perfect ($r_p = 1$) coincidences, whereas Kolyma basin show $r_p$ below 0,5 (0.4). Overall, the ECA results show high coincidences between SPI anomalies and FracSA BPs in most of world's large basins. However, one should be aware of the potential uncertainty associated with FracSA values in high-latitude basins during winter months due to the low observation rate of Landsat.

### 3.4. Discussion

At monthly scale, we find more than half (52.7%) of the global riverine area is covered by water less than half of the time. This finding should be interpreted and conditioned on our definition of the examination extent, i.e., the maximum river extent, which is designed to cover all locations with water detected at least once during the examination period (1985 to 2015) and to encompass the full spectrum of river extent. Like streamflow, river extent is positively skewed in its temporal distribution, consisting of more small values than large values, which means the median river extent (corresponding to SWP $\geq$50%) should cover less than 50% of the maximum river extent. Interestingly, the year-based calculation favors the number of with-water years and causes river extent to be negatively skewed: only 22.2% of river extent is covered by water less than half of the time based on year-based SWP.

The maximum river extent encompasses not only the riverine responses to the hydro-meteorologic/hydro-climatic factors but also geomorphological processes. Fig. 11 illustrates the shift of rivers'

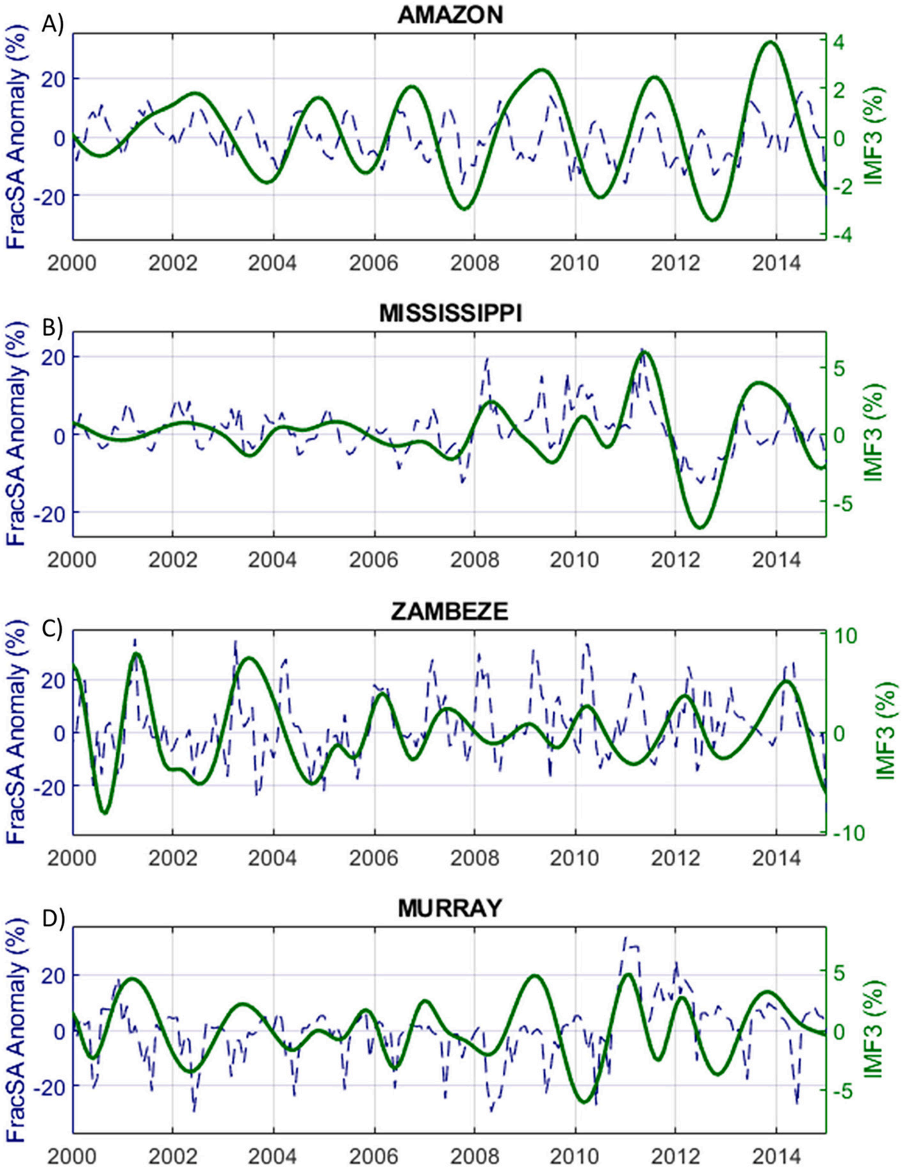

**Fig. 8.** Time series of the FracSA anomaly and its third intrinsic mode function (IMF3) for (A) Amazon, (B) Mississippi, (B) Zambeze, and (D) Murray Darling river basins.

meandering pattern over time at three locations in Amazon basin. Across a twenty-year gap between 1994 and 2014, rivers in July of 2014 (green plus black area) appear to be very different from those in July of 1994 (red plus black area). At all three locations, we see cases of increased channel sinuosity over time and cutoffs formed at the meandering neck. Although the geomorphological process is pronounced at local scale, calculation of FracSA of large river basins likely diffuses such effects. In fact, the FracSA values in Amazon at the two times are very similar, i.e., 0.687 in 07/1994 and 0.702 in 07/2014, respectively.

The findings of this study have implications on hydrologic modeling and forecasting of global rivers. The correlation analysis suggests that importance of low-flow-generating processes, e.g., snow-melting, infiltration, and recharge-discharge. This can also be explained by the positively skewed nature of streamflow where low-moderate flow as the majority originates from groundwater and snowpack. In spite of the prevalence of these processes, they are not yet represented sufficiently by the state-of-the-art hydrologic models (Lin et al., 2019), especially in the subsurface layers. The challenges include the lack of information on bedrock properties and topography and the difficulty to assign spatially and vertically distributed parameters (Camporese et al., 2019). Moreover, we expect the significance of low-flow-generating processes to be greater than what this study reveals, because the Landsat observation can only capture rivers wider than 30 m, missing most non-perennial headwater streams (Palmer and Ruhi, 2018) whose dynamics are even more dependent on low flow (Gao et al., 2021a). Finally, the correlation analysis demonstrates the precedence of TWS over FracSA in certain river basins. For instance, the correlation coefficients between FracSA and TWS are 0.625 in Amazon with 3 months of lagging, 0.57 in Murray Darling with 3 months of lagging, and 0.72 in Kolyma with 2 months of lagging. This indicates potential predictability of the river water from GRACE observation with months of lead time. Reager et al. (2014) demonstrated the similar finding by correlating GRACE observation with gauge measurements to infer predictability of flood potential.

## 4. Conclusions

In this study, we examine the spatiotemporal dynamics of surface water in rivers based on Landsat observations and investigate the corresponding natural driving factors. Through the combined usage of

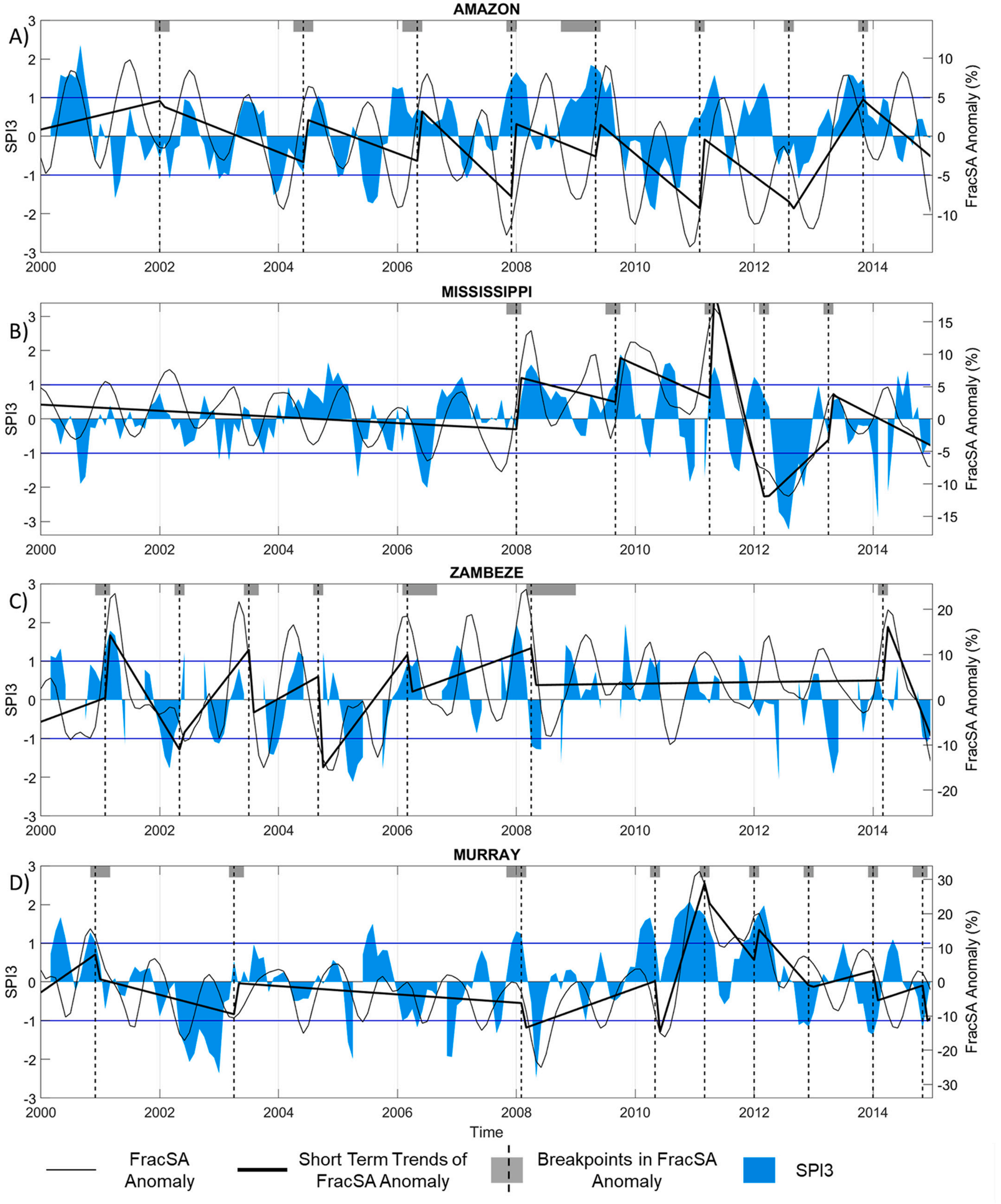

**Fig. 9.** BPs detected in FracSA of (A) Amazon, (B) Mississippi, (C) Zambeze, and (D) Murray Darling river basins. Left axis: SPI (filled blue areas) and ± 1 SPI thresholds (horizontal blue lines); right axis: FracSA anomalies (thin gray line), BFAST trends (bold black line), breakpoints (vertical dotted line), confidence intervals (light gray shades). (For interpretation of the references to colour in this figure legend, the reader is referred to the web version of this article.)

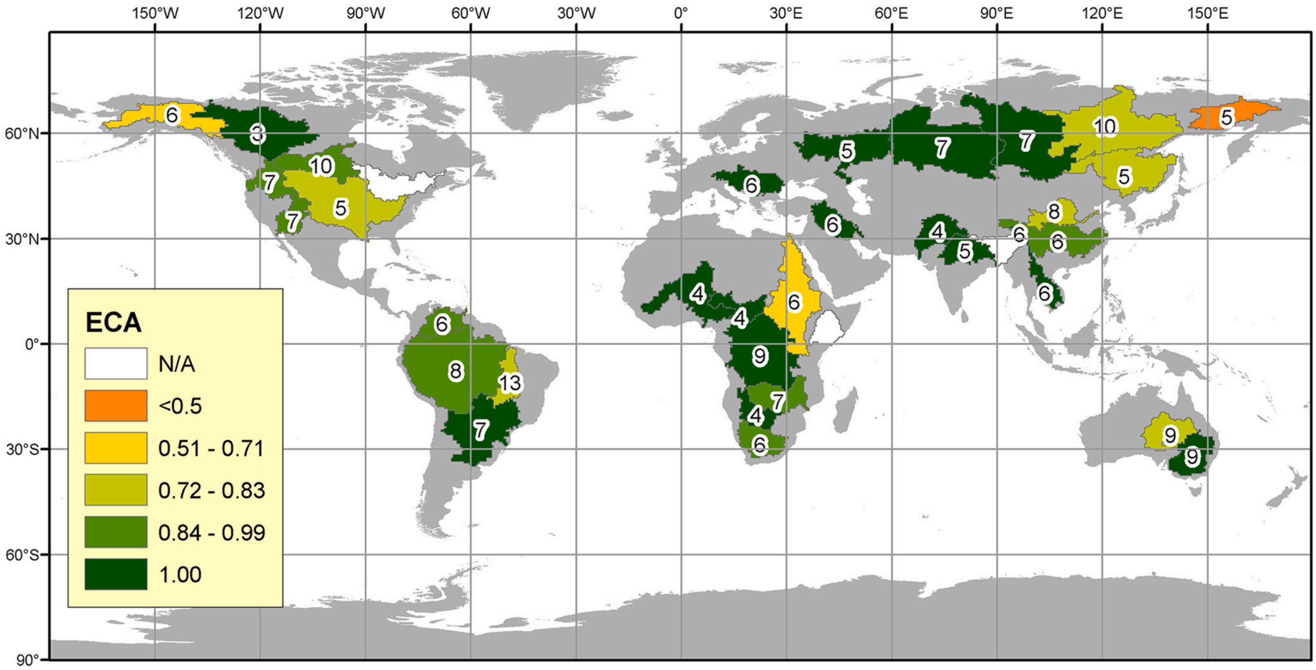

**Fig. 10.** Precursor coincidence rates between BPs of FracSA and SPI anomalies for 35 river basins. Labels signify number of BPs in FracSA time series.

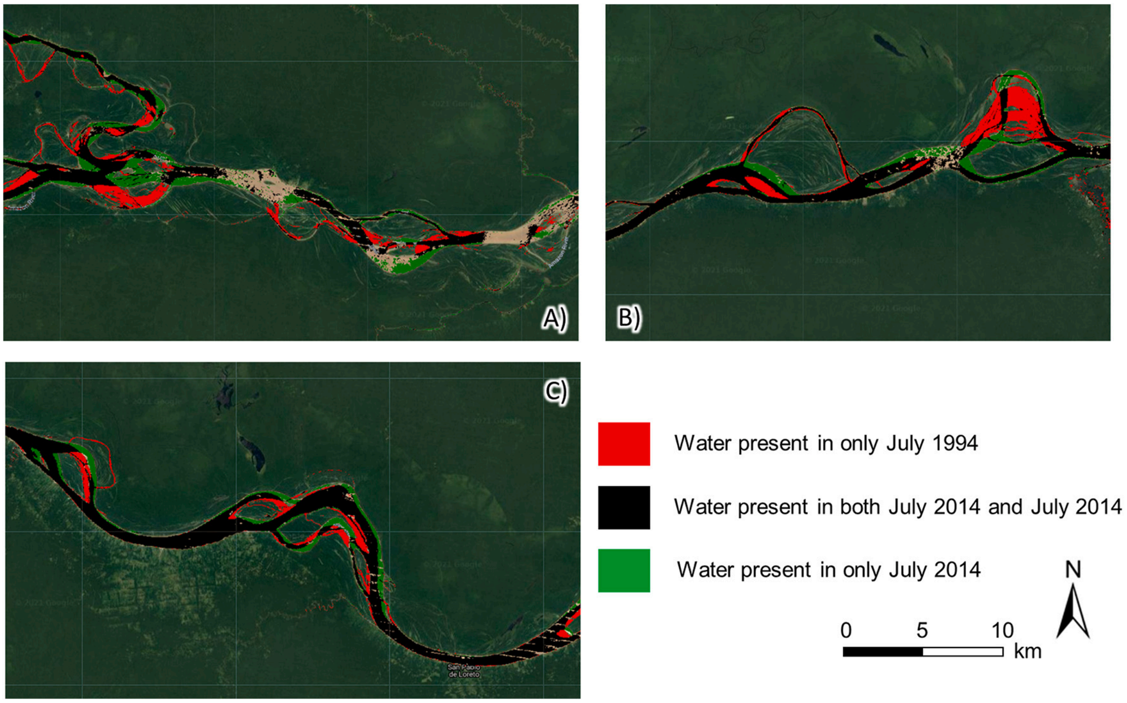

**Fig. 11.** Examples of river channel shifts in Amazon based on GSW monthly history product in July of 1994 and July of 2014 at (A) -72.5°, −3.4°, (B) -70.8°, −3.9°, and (C) -68.5°, −3.4°. The colors are only shown for confined regions of the finalized maximum river extent as defined in this study.

GRWL centerline vectors and GSW monthly history observation, we define an examination extent that covers the full variabilities of river dynamics over a 30-year period from 1985 to 2015. Within this maximum river extent, we first produce long-term mean surface water presence in global rivers and investigate the spatial patterns among various climate zones. We also offer an innovative perspective to study river dynamics by correlating the fractional river extent (FracSA) with TWS components extracted from the GRACE observation and the GLDAS simulation in world's large river basins. Lastly, the extremes of FracSA are associated with precipitation anomalies via the event coincidence analysis (ECA), in which an EMD-aided BP-detection method is explored to identify the non-stationary and irregular FracSA extremes. The specific findings of this study are summarized as follows:

1. At monthly scale, 52.7% of global maximum river extent is covered by water less than half of the time (SWP $< 50\%$). The spatiotemporal variability of river extent can be well explained via differentiating climate zones. Water in cold, high-latitude areas has high presence in

numerous rivers due to the slow snow-melting process and low evapotranspiration. Rivers in arid climates feature rare presence and small surface extent due to low precipitation as sources and high evapotranspiration (temperature) as sinks.

2. In world's large river basins, fractional river extent (FracSA) is fairly correlated with Terrestrial Water Storage components (GWS, SoilMoist_RZ, and CanopInt) in low- and mid-latitudes. The optimized lags in the correlation analysis indicate GWS precedes FracSA most closely, followed by SoilMoist_RZ and then CanopInt, which suggests strong controls of subsurface processes (infiltration and recharge-discharge) on river dynamics in low- and mid-latitudes. In high latitudes, the drop of SWE corresponds to the increases of GWS, SoilMoist_RZ and FracSA in spring due to snow melting.
3. The EMD-aided BP detection is adaptive and flexible in identifying FracSA extremes occurring at irregular intervals. The event coincidence of FracSA extremes with SPI anomalies shows precipitation as hydrologic inputs are potential driving factors for abrupt changes of FracSA in equatorial, arid, and warm temperate areas.
4. The correlation analysis and ECA together demonstrate the roles of various hydrologic processes on flow regimes. Controlled by the subsurface runoff, groundwater and snow melting, the low-moderate flow regimes constitute significant portion of global river dynamics. The extremes in river dynamics (wet and dry events) are associated more with precipitation anomalies. High precipitation as the source of surface runoff generates large streamflow during floods, whereas extended no-rain periods leave rivers to dry during droughts.

Although this study validates that hydrometeorological processes have first-order controls over river dynamics, the river basin scale likely dilutes other local factors. The areal averaging lessens the effects from geomorphological processes like change in river meandering pattern over time. Also, flow regulation, like damming and flow diversion, is very typical in arid regions with high water-stress where large percentage of exploitable flow is often extracted for irrigation use (Vörösmarty et al., 2010). Hammond et al. (2020) demonstrated combinations of climatic, physiographic and anthropogenic drivers emerged at regional scales affect non-perennial flow regimes across the Contiguous United States. Therefore, future research is still needed to disentangle various anthropogenic and geomorphological factors on the river dynamics at local/regional scales. In addition, to better characterize and interpret the extremes in river dynamics, hydrologic and hydraulic simulations can fill the spatiotemporal gaps in the Landsat observations and explicitly attribute the extremes of river dynamics based on model fluxes and states.

## Declaration of Competing Interest

The authors declare that they have no known competing financial interests or personal relationships that could have appeared to influence the work reported in this paper.

## Acknowledgment

This work was supported by funding from the US National Science Foundation (Project number: 1802872). We appreciate valuable comments from three anonymous reviewers who greatly help improve the overall quality of this work.

## References

Abbott, B.W., Bishop, K., Zarnetske, J.P., Minaudo, C., Chapin, F., Krause, S., Hannah, D. M., Conner, L., Ellison, D., Godsey, S.E., 2019. Human domination of the global water cycle absent from depictions and perceptions. Nat. Geosci. 12, 533–540.

Ahmed, M., Sultan, M., Wahr, J., Yan, E., 2014. The use of GRACE data to monitor natural and anthropogenic induced variations in water availability across Africa. Earth Sci. Rev. 136, 289–300.

Allen, G.H., Pavelsky, T.M., 2018. Global extent of rivers and streams. Science 361, 585–588.

Allen, G.H., Yang, X., Gardner, J., Holliman, J., David, C.H., Ross, M., 2020. Timing of Landsat overpasses effectively captures flow conditions of large rivers. Remote Sens. 12, 1510.

Azzari, G., Lobell, D., 2017. Landsat-based classification in the cloud: an opportunity for a paradigm shift in land cover monitoring. Remote Sens. Environ. 202, 64–74.

Bastviken, D., Tranvik, L.J., Downing, J.A., Crill, P.M., Enrich-Prast, A., 2011. Freshwater methane emissions offset the continental carbon sink. Science 331, 50.

Camporese, M., Paniconi, C., Putti, M., McDonnell, J.J., 2019. Fill and spill hillslope runoff representation with a Richards equation-based model. Water Resour. Res. 55, 8445–8462.

Chen, J., Wilson, C., Tapley, B., Yang, Z., Niu, G.-Y., 2009. 2005 drought event in the Amazon River basin as measured by GRACE and estimated by climate models. J. Geophys. Res. Solid Earth 114.

Chen, J.L., Wilson, C.R., Tapley, B.D., 2010. The 2009 exceptional Amazon flood and interannual terrestrial water storage change observed by GRACE. Water Resour. Res. 46.

CRED, 2017. EM-DATA. In: C.f.R.o.t.E.o. Disasters (Ed.), The International Disaster Database. Université Catholique de Louvain, Louvain-la-Neuve, Belgium.

Crowley, J.W., Mitrovica, J.X., Bailey, R.C., Tamisiea, M.E., Davis, J.L., 2006. Land water storage within the Congo Basin inferred from GRACE satellite gravity data. Geophys. Res. Lett. 33.

Donchyts, G., Baart, F., Winsemius, H., Gorelick, N., Kwadijk, J., Van De Giesen, N., 2016. Earth's surface water change over the past 30 years. Nat. Clim. Chang. 6, 810–813.

Espinoza, J.C., Ronchail, J., Frappart, F., Lavado, W., Santini, W., Guyot, J.L., 2013. The major floods in the Amazonas River and tributaries (Western Amazon basin) during the 1970–2012 period: a focus on the 2012 flood. J. Hydrometeorol. 14, 1000–1008.

Fekete, B.M., Robarts, R.D., Kumagai, M., Nachtnebel, H.-P., Odada, E., Zhulidov, A.V., 2015. Time for in Situ Renaissance.

Forootan, E., Schumacher, M., Awange, J.L., Müller Schmied, H., 2016. Exploring the influence of precipitation extremes and human water use on total water storage (TWS) changes in the G anges-B rahmaputra-M eghna River Basin. Water Resour. Res. 52, 2240–2258.

Frappart, F., Ramillien, G., Ronchail, J., 2013. Changes in terrestrial water storage versus rainfall and discharges in the Amazon basin. Int. J. Climatol. 33, 3029–3046.

Gao, S., Chen, M., Li, Z., Cook, S., Allen, D., Neeson, T., Yang, T., Yami, T., Hong, Y., 2021a. Mapping dynamic non-perennial stream networks using high-resolution distributed hydrologic simulation: a case study in the upper blue river basin. J. Hydrol. 126522.

Gao, S., Li, Z., Chen, M., Allen, D., Neeson, T., Hong, Y., 2021b. Monitoring drought through the lens of Landsat: drying of rivers during the California droughts. Remote Sens. 13 (17), 3423.

Gleason, C.J., Smith, L.C., 2014. Toward global mapping of river discharge using satellite images and at-many-stations hydraulic geometry. Proc. Natl. Acad. Sci. 111, 4788–4791.

Gorelick, N., Hancher, M., Dixon, M., Ilyushchenko, S., Thau, D., Moore, R., 2017. Google earth engine: planetary-scale geospatial analysis for everyone. Remote Sens. Environ. 202, 18–27.

Gudmundsson, L., Leonard, M., Do, H.X., Westra, S., Seneviratne, S.I., 2019. Observed trends in global indicators of mean and extreme streamflow. Geophys. Res. Lett. 46, 756–766.

Hammond, J.C., Zimmer, M., Shanafield, M., Kaiser, K., Godsey, S.E., Mims, M.C., Zipper, S.C., Burrows, R.M., Kampf, S.K., Dodds, W., 2020. Spatial patterns and drivers of non-perennial flow regimes in the contiguous US. Geophys. Res. Lett. 48 (2), e2020GL090794.

Hodgkins, G.A., Whitfield, P.H., Burn, D.H., Hannaford, J., Renard, B., Stahl, K., Fleig, A. K., Madsen, H., Mediero, L., Korhonen, J., 2017. Climate-driven variability in the occurrence of major floods across North America and Europe. J. Hydrol. 552, 704–717.

Hoerling, M., Eischeid, J., Kumar, A., Leung, R., Mariotti, A., Mo, K., Schubert, S., Seager, R., 2014. Causes and predictability of the 2012 Great Plains drought. Bull. Am. Meteorol. Soc. 95, 269–282.

Hou, J., van Dijk, A.I., Beck, H.E., 2020. Global satellite-based river gauging and the influence of river morphology on its application. Remote Sens. Environ. 239, 111629.

Huang, N.E., Shen, Z., Long, S.R., Wu, M.C., Shih, H.H., Zheng, Q., Yen, N.-C., Tung, C.C., Liu, H.H., 1998. The empirical mode decomposition and the Hilbert spectrum for nonlinear and non-stationary time series analysis. Proc. Royal Soc. Lond. Ser. A: Math. Phys. Eng. Sci. 454, 903–995.

Jensen, C.K., McGuire, K.J., Prince, P.S., 2017. Headwater stream length dynamics across four physiographic provinces of the A ppalachian H ighlands. Hydrol. Process. 31, 3350–3363.

Kottek, M., Grieser, J., Beck, C., Rudolf, B., Rubel, F., 2006. World map of the Köppen-Geiger climate classification updated. Meteorol. Z. 15, 259–263.

Leblanc, M., Tweed, S., Van Dijk, A., Timbal, B., 2012. A review of historic and future hydrological changes in the Murray-Darling basin. Glob. Planet. Chang. 80, 226–246.

Lehner, B., Grill, G., 2013. Global river hydrography and network routing: baseline data and new approaches to study the world's large river systems. Hydrol. Process. 27, 2171–2186.

Lin, P., Pan, M., Beck, H.E., Yang, Y., Yamazaki, D., Frasson, R., David, C.H., Durand, M., Pavelsky, T.M., Allen, G.H., 2019. Global reconstruction of naturalized river flows at 2.94 million reaches. Water Resour. Res. 55, 6499–6516.

Maeda, E.E., Kim, H., Aragão, L.E., Famiglietti, J.S., Oki, T., 2015. Disruption of hydroecological equilibrium in southwest Amazon mediated by drought. Geophys. Res. Lett. 42, 7546–7553.

Messager, M.L., Lehner, B., Grill, G., Nedeva, I., Schmitt, O., 2016. Estimating the volume and age of water stored in global lakes using a geo-statistical approach. Nat. Commun. 7, 1–11.

Mueller, N., Lewis, A., Roberts, D., Ring, S., Melrose, R., Sixsmith, J., Lymburner, L., McIntyre, A., Tan, P., Curnow, S., 2016. Water observations from space: mapping surface water from 25 years of Landsat imagery across Australia. Remote Sens. Environ. 174, 341–352.

Oki, T., Sud, Y., 1998. Design of Total Runoff Integrating Pathways (TRIP)—a global river channel network. Earth Interact. 2, 1–37.

Palmer, M., Ruhi, A., 2018. Measuring Earth's rivers. Science 361, 546–547.

Pavelsky, T.M., 2014. Using width-based rating curves from spatially discontinuous satellite imagery to monitor river discharge. Hydrol. Process. 28, 3035–3040.

Pekel, J.-F., Cottam, A., Gorelick, N., Belward, A.S., 2016. High-resolution mapping of global surface water and its long-term changes. Nature 540, 418–422.

Raymond, P.A., Hartmann, J., Lauerwald, R., Sobek, S., McDonald, C., Hoover, M., Butman, D., Striegl, R., Mayorga, E., Humborg, C., 2013. Global carbon dioxide emissions from inland waters. Nature 503, 355–359.

Reager, J., Thomas, B., Famiglietti, J., 2014. River basin flood potential inferred using GRACE gravity observations at several months lead time. Nat. Geosci. 7, 588–592.

Rodell, M., Houser, P., Jambor, U., Gottschalck, J., Mitchell, K., Meng, C.-J., Arsenault, K., Cosgrove, B., Radakovich, J., Bosilovich, M., 2004. The global land data assimilation system. Bull. Am. Meteorol. Soc. 85, 381–394.

Save, H., Bettadpur, S., Tapley, B.D., 2016. High-resolution CSR GRACE RL05 mascons. J. Geophys. Res. Solid Earth 121, 7547–7569.

Shaw, S.B., 2016. Investigating the linkage between streamflow recession rates and channel network contraction in a mesoscale catchment in New York state. Hydrol. Process. 30, 479–492.

Sichangi, A.W., Wang, L., Yang, K., Chen, D., Wang, Z., Li, X., Zhou, J., Liu, W., Kuria, D., 2016. Estimating continental river basin discharges using multiple remote sensing data sets. Remote Sens. Environ. 179, 36–53.

Siegmund, J.F., Siegmund, N., Donner, R.V., 2017. CoinCalc—A new R package for quantifying simultaneities of event series. Comput. Geosci. 98, 64–72.

Sun, A.Y., Scanlon, B.R., AghaKouchak, A., Zhang, Z., 2017. Using GRACE satellite gravimetry for assessing large-scale hydrologic extremes. Remote Sens. 9, 1287.

Tananaev, N., Makarieva, O., Lebedeva, L., 2016. Trends in annual and extreme flows in the Lena River basin, Northern Eurasia. Geophys. Res. Lett. 43, 10,764–710,772.

Tang, Q., Gao, H., Lu, H., Lettenmaier, D.P., 2009. Remote sensing: hydrology. Prog. Phys. Geogr. 33, 490–509.

Tarpanelli, A., Santi, E., Tourian, M.J., Filippucci, P., Amarnath, G., Brocca, L., 2018. Daily river discharge estimates by merging satellite optical sensors and radar altimetry through artificial neural network. IEEE Trans. Geosci. Remote Sens. 57, 329–341.

Tourian, M., Schwatke, C., Sneeuw, N., 2017. River discharge estimation at daily resolution from satellite altimetry over an entire river basin. J. Hydrol. 546, 230–247.

Van Dijk, A.I., Brakenridge, G.R., Kettner, A.J., Beck, H.E., De Groeve, T., Schellekens, J., 2016. River gauging at global scale using optical and passive microwave remote sensing. Water Resour. Res. 52, 6404–6418.

Verbesselt, J., Hyndman, R., Newnham, G., Culvenor, D., 2010. Detecting trend and seasonal changes in satellite image time series. Remote Sens. Environ. 114, 106–115.

Vicente-Serrano, S.M., Beguería, S., López-Moreno, J.I., 2010. A multiscalar drought index sensitive to global warming: the standardized precipitation evapotranspiration index. J. Clim. 23, 1696–1718.

Vörösmarty, C.J., McIntyre, P.B., Gessner, M.O., Dudgeon, D., Prusevich, A., Green, P., Glidden, S., Bunn, S.E., Sullivan, C.A., Liermann, C.R., 2010. Global threats to human water security and river biodiversity. Nature 467, 555–561.

Winsemius, H., Savenije, H., Van De Giesen, N., Van Den Hurk, B., Zapreeva, E., Klees, R., 2006. Assessment of gravity recovery and climate experiment (GRACE) temporal signature over the upper Zambezi. Water Resour. Res. 42.

Wu, Z., Huang, N.E., 2004. A study of the characteristics of white noise using the empirical mode decomposition method. Proc. Royal Soc. Lond. Ser. A: Math. Phys. Eng. Sci. 460, 1597–1611.

Wulder, M.A., White, J.C., Loveland, T.R., Woodcock, C.E., Belward, A.S., Cohen, W.B., Fosnight, E.A., Shaw, J., Masek, J.G., Roy, D.P., 2016. The global Landsat archive: status, consolidation, and direction. Remote Sens. Environ. 185, 271–283.

Yamazaki, D., Lee, H., Alsdorf, D.E., Dutra, E., Kim, H., Kanae, S., Oki, T., 2012. Analysis of the water level dynamics simulated by a global river model: a case study in the Amazon River. Water Resour. Res. 48.

Yamazaki, D., O'Loughlin, F., Trigg, M.A., Miller, Z.F., Pavelsky, T.M., Bates, P.D., 2014. Development of the global width database for large rivers. Water Resour. Res. 50, 3467–3480.

Yang, X., Pavelsky, T.M., Allen, G.H., Donchyts, G., 2019. RivWidthCloud: an automated Google earth engine algorithm for river width extraction from remotely sensed imagery. IEEE Geosci. Remote Sens. Lett. 17, 217–221.

Yang, J., Huang, X., Tang, Q., 2020. Satellite-derived river width and its spatiotemporal patterns in China during 1990–2015. Remote Sens. Environ. 247, 111918.